

Dysprosium doping of Ca_2MnO_4 : Effect on crystal structure at room temperature and thermal behavior

D. Bregiroux^{1,*}, A. Bahezre¹, M. Allani¹, G. Rousse², G. Wallez³, and C. Laberty-Robert¹

¹ Sorbonne Université, CNRS, Chimie de la Matière Condensée de Paris, LCMCP, F-75005 Paris, France

² Sorbonne Université, Collège de France, UMR 8260 Chimie du Solide et de l'Énergie (CSE), 75231 Paris Cedex 05, France

³ Sorbonne Université, UFR 926, 75005 Paris, France ; Chimie ParisTech, Université PSL, CNRS, Institut de Recherche de Chimie Paris (IRCP), UMR 8247, 11 rue P. et M. Curie, 75005 Paris, France

* Corresponding author. Tel.: + 331 442 75679

E-mail address: damien.bregiroux@sorbonne-universite.fr (D. Bregiroux)

Abstract

Dysprosium-doped Ruddlesden–Popper calcium manganates with compositions of $\text{Ca}_{2-x}\text{Dy}_x\text{MnO}_4$ are potential candidates for high temperature thermoelectric applications. The effect of dysprosium doping on the crystal structure of $\text{Ca}_{2-x}\text{Dy}_x\text{MnO}_4$ at room temperature and its thermal behavior between RT and 800 °C were investigated in the range $0 < x < 0.2$ by Rietveld analysis of RT- and HT- X-ray powder diffraction data. The Rietveld analysis confirmed the compatibility of all the analyzed compounds with the $I4_1/acd$ space group. Ca^{2+} substitution by Dy^{3+} , electrically balanced by the reduction of an equivalent amount of Mn^{4+} to Mn^{3+} , leads to an increase of the a parameter and a decrease of the c parameter. No phase

transition was observed from RT to 800 °C but we show that several complex structural mechanisms lead to a strong anisotropic thermal expansion.

Keywords

Ruddlesden-Popper phases; Calcium manganates; Crystal structure; Rietveld analysis; Thermal expansion

1. Introduction

Compounds in the $\text{CaO-Mn}^{\text{IV}}\text{O}_2$ system have received wide attention of researchers since several decades as they are promising candidates for various applications. They can be used as near-IR reflective black pigments [1], magnetic [2,3], dielectric [4,5,6,7], electrochemical [8] and thermoelectric materials [9,10,11]. Even though CaMnO_3 is the most investigated end-member, the compounds with the general formula $\text{CaO}(\text{CaMnO}_3)_n$ ($n = 1, 2, \dots, \infty$), *i.e.* the so-called Ruddlesden-Popper phases (RP), also exhibit very interesting properties [12,13,14]. As illustrated on Fig. 1, the Ruddlesden Popper phase structure is built up by alternating n perovskite CaMnO_3 layers with a rock-salt CaO layer [15]. For all compositions, perovskite layers are made of 2D or 3D arrays of corner sharing MnO_6 octahedra. For the CaMnO_3 end member, the coordination of the calcium cation is 12, whereas it is 11 for $\text{Ca}_3\text{Mn}_2\text{O}_7$ and 9 for Ca_2MnO_4 .

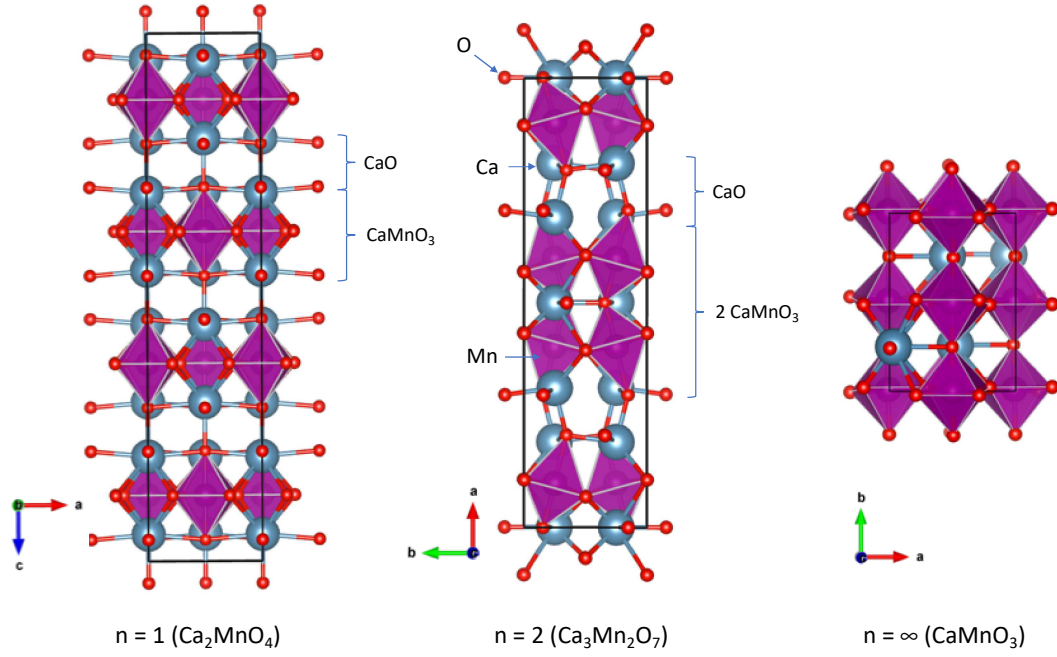
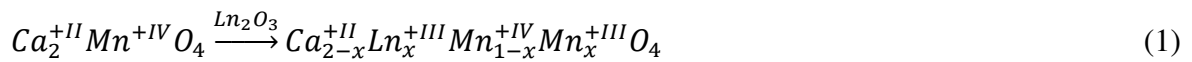


Fig. 1. Crystal structures of $\text{CaO}(\text{CaMnO}_3)_n$ for $n = 1, 2$ and ∞ .

For thermoelectric applications, in order to obtain high value of Figure of Merit (ZT), electrical conductivity of calcium manganates can be enhanced by doping with heterovalent cations, *e.g.* with trivalent lanthanide elements (Ln^{3+}) on the Ca^{2+} sites [16]. Considering the statement of Takahashi and Kamegashira who showed that oxygen nonstoichiometry in Ca_2MnO_4 significantly appeared above about 1200K and was reversible up to 1600K [17], one can consider that electrical neutrality should be achieved by the reduction of an equivalent amount of Mn^{4+} to Mn^{3+} , according to the following equation:



The electronic conduction then occurs by a hopping mechanism between Mn^{3+} and Mn^{4+} , as demonstrated by Chaumont *et al.* in 1975 [18]. The results obtained on $\text{Ca}_{1-x}\text{Ln}_x\text{MnO}_3$ perovskite ($n = \infty$) highlighted that best ZT values are achieved for $\text{Ln} = \text{Dy}$ and $x=0.02$ [19,20]. Considering that a similar behavior should certainly be observed for Ruddlesden-Popper calcium manganates, the objective of the present work is to investigate the crystal modification induced by Dy doping in $\text{Ca}_{2-x}\text{Dy}_x\text{MnO}_4$ compound in the range $0 < x < 0.2$ at

room temperature. Phase stability and thermal expansion are expected to be important during processing and in operation. Consequently, thermal behavior of the $\text{Ca}_{1.8}\text{Dy}_{0.2}\text{MnO}_4$ structure is also investigated for the first time by HT-XRD between room temperature to 800 °C.

2. Experimental details

Ruddlesden-Popper-type layered perovskites $\text{Ca}_{2-x}\text{Dy}_x\text{MnO}_4$ ($x = 0, 0.04, 0.1, 0.2$) were prepared by the auto-combustion method. Stoichiometric amounts of $\text{Ca}(\text{NO}_3)_2 \cdot 4\text{H}_2\text{O}$, $\text{Dy}(\text{NO}_3)_3 \cdot 5\text{H}_2\text{O}$, and $\text{Mn}(\text{NO}_3)_2 \cdot 4\text{H}_2\text{O}$ (Alfa Aesar, purity > 98 %) were dissolved in ultrapure water with citric acid $\text{C}_6\text{H}_8\text{O}_7 \cdot \text{H}_2\text{O}$ (7 molar equivalent *vs.* Mn) in a huge beaker (typically 5 L for a 200 mL initial mixture). The solution was dried at 130 °C for 10 h. Upon removal from the oven, the beaker was filled completely with a pale-brown foam. This foam was then gently crushed by ball-milling at 80 rpm for 1 night to decrease its volume, before being heated under a strong air flow ($> 1 \text{ L} \cdot \text{min}^{-1}$) at 850 °C for 4 h with a $5 \text{ }^\circ\text{C} \cdot \text{min}^{-1}$ heating rate. The final powder was deep black. TEM observations highlighted that the powder consists in rosary-like hard agglomerates made of well-crystallized 50-80 nm nanoparticles (Fig. 2). All the synthesized powders exhibit the same morphology, whatever the Dy doping level.

X-ray powder diffraction (XRD) was performed with a Bruker D8 Advance diffractometer in Bragg-Brentano θ - θ geometry with a $\text{CuK}\alpha$ source ($\lambda \text{ K}\alpha_1 = 1.54056 \text{ \AA}$, $\lambda \text{ K}\alpha_2 = 1.54439 \text{ \AA}$). Powder patterns were collected in the 2θ range 8-120° with a 0.02° step. High temperature XRD was performed using an Anton Paar HTK 1200N furnace. Rietveld analysis was performed using the FullProf Suite software [21].

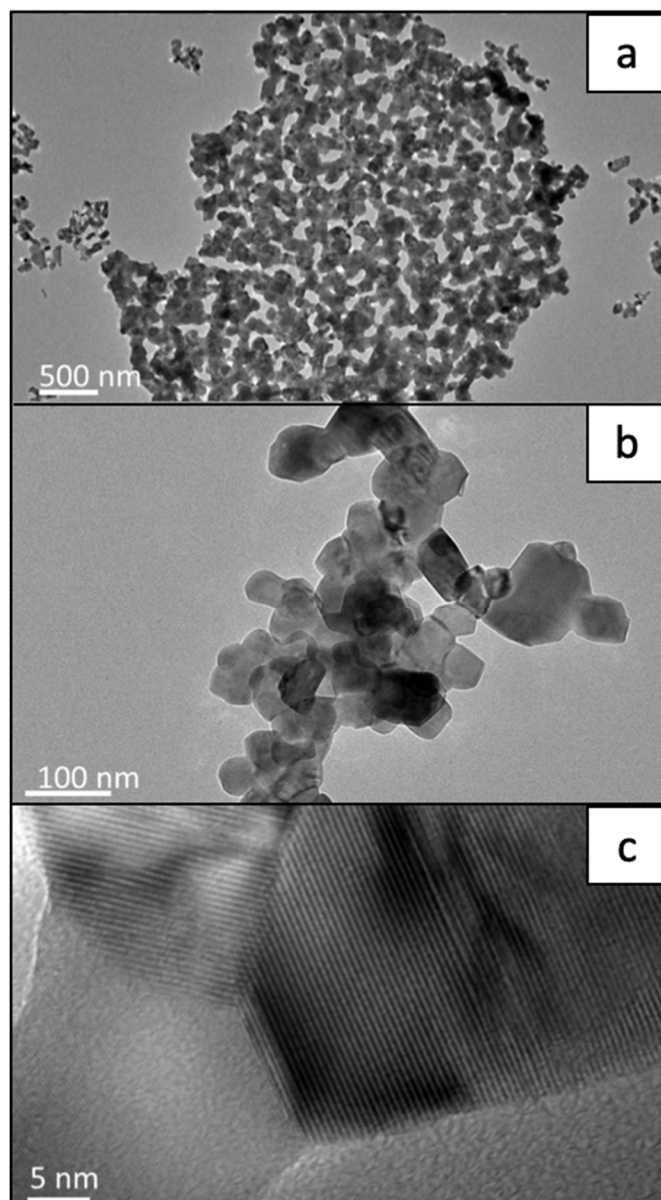


Fig. 2. TEM micrographs of the synthesized Ca_2MnO_4 powder

3. Results and discussion

3.1. Structure modifications at room temperature

Except for very minor reflections ascribed to the perovskite CaMnO_3 , all the synthesized powders XRD patterns are consistent with that previously reported for Ca_2MnO_4 compounds and indicate the presence of a $\text{Ca}_{2-x}\text{Dy}_x\text{MnO}_4$ solid solution at least up to $x=0.2$ [22]. All patterns can be indexed in the $I4_1/acd$ space group with lattice parameters ($a = 5.1921(2) \text{ \AA}$, $c = 24.091(2) \text{ \AA}$ for $x = 0$). Rietveld refinements were undertaken on all samples, with an initial

model built on the atomic positions of Ca_2MnO_4 published by Autret *et al.* [23] with Dy on the Ca site. For the refinement, the background was modeled by an interpolation of points, the peak shape was described by a Thompson-Cox-Hastings pseudo-Voigt function convoluted with axial divergence asymmetry function [24]. All atomic positions and isotropic B's were refined. An example of final Rietveld refinement, obtained for $\text{Ca}_{2-x}\text{Dy}_x\text{MnO}_4$ with $x = 0.1$, is shown in Fig. 3. The refinement parameters and the obtained crystallographic data are reported in Table 1 and Table 2. Reliability factors appears to be good enough to retrieve the influence of the Dy doping level on the length of the cation-oxygen bonds. All the results are plotted in the 8 graphs of Fig. 4 and illustrated on the crystal structure of Ca_2MnO_4 in Fig. 5.

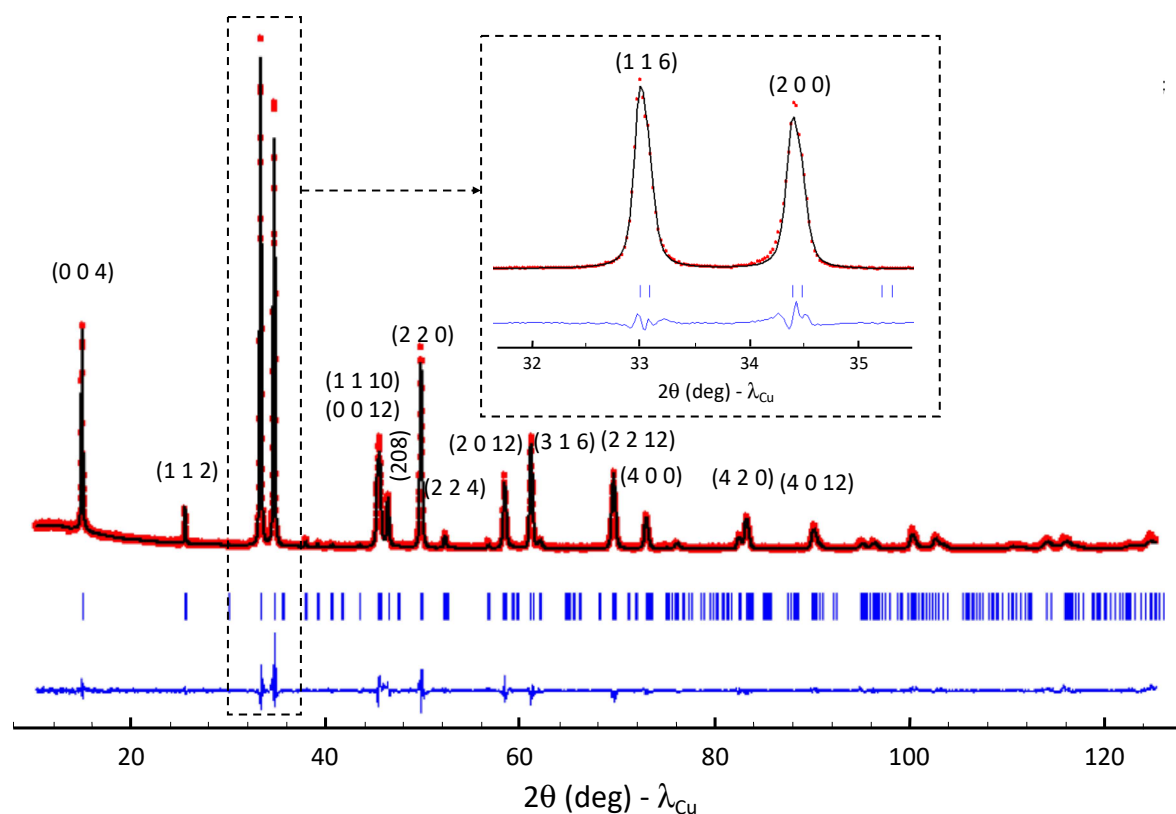


Fig. 3. Rietveld refinement for $\text{Ca}_{1.9}\text{Dy}_{0.1}\text{MnO}_4$: y_{obs} (red dots), y_{calc} (black solid line, upper), $y_{\text{obs}} - y_{\text{calc}}$ (blue solid line, lower), Bragg positions (blue bars).

Table 1

Main acquisition, refinement and lattice data for undoped and Dy-doped Ca_2MnO_4

Sample	Ca_2MnO_4	$\text{Ca}_{1.96}\text{Dy}_{0.04}\text{MnO}_4$	$\text{Ca}_{1.90}\text{Dy}_{0.10}\text{MnO}_4$	$\text{Ca}_{1.80}\text{Dy}_{0.20}\text{MnO}_4$
Measured reflections	224	281	314	323
Fitted parameters	25	26	26	26
Reliability factors	$R_{\text{Bragg}} = 0.053$ $\chi^2 = 4.59$	$R_{\text{Bragg}} = 0.082$ $\chi^2 = 2.28$	$R_{\text{Bragg}} = 0.066$ $\chi^2 = 2.64$	$R_{\text{Bragg}} = 0.057$ $\chi^2 = 2.42$
System	Tetragonal	Tetragonal	Tetragonal	Tetragonal
Space group	$I4_1/acd$ (142)	$I4_1/acd$ (142)	$I4_1/acd$ (142)	$I4_1/acd$ (142)
Cell parameters (Å)	a = 5.1922(2)	a = 5.2060(2)	a = 5.2269(1)	a = 5.2558(3)
Volume (Å ³)	c = 24.095(2) V = 649.57(3)	c = 24.033(1) V = 651.35(4)	c = 23.937(1) V = 653.96(4)	c = 23.822(2) V = 658.04(2)
Formula per cell/calc. density (g.cm ⁻³)	8/4.07	8/4.15	8/4.30	8/4.48

Table 2

Atomic parameters and thermal factors for undoped and Dy-doped Ca_2MnO_4 . B_{iso} 's were imposed the same for a same chemical species.

	atom	Wyckoff	x	y	z	B_{iso} (Å ²)
Ca_2MnO_4	Mn	8a	0	0	0	0.417(76)
	Ca	16d	0	0	0.1756(1)	0.531(48)
	O3	16d	0	0	0.0814(3)	0.950(104)
	O4	16f	0.2114(10)	0.2114(10)	0.25	0.950(104)
$\text{Ca}_{1.96}\text{Dy}_{0.04}\text{MnO}_4$	Mn	8a	0	0	0	0.242(57)
	Ca/Dy	16d	0	0	0.1760(1)	0.698(52)
	O3	16d	0	0	0.0810(4)	0.776(84)
	O4	16f	0.2155(20)	0.2155(20)	0.25	0.776(84)
$\text{Ca}_{1.9}\text{Dy}_{0.1}\text{MnO}_4$	Mn	8a	0	0	0	0.361(73)
	Ca/Dy	16d	0	0	0.1763(9)	0.831(58)
	O3	16d	0	0	0.0813(6)	0.960(107)
	O4	16f	0.2179(10)	0.2179(10)	0.25	0.960(107)
$\text{Ca}_{1.8}\text{Dy}_{0.2}\text{MnO}_4$	Mn	8a	0	0	0	0.357(88)
	Ca/Dy	16d	0	0	0.1764(2)	0.881(61)
	O3	16d	0	0	0.0819(6)	1.244(123)
	O4	16f	0.2250(20)	0.2250 (20)	0.25	1.244(123)

Table 3

Bond lengths and angles values of undoped Ca_2MnO_4 at RT

Bond/angle		Bond/angle	
Ca-O3	2.2720(6) Å (x2) [100]	Mn-O3	1.9610(4) Å (x2)
	2.6017(1) Å (x4) \perp [100]		
Ca-O4	2.7648(2) Å (x2)	Mn-O4	1.8557(0) Å (x4)
	2.3768(3) Å (x2)		

O3-Ca-O3	172.45(12) (°)	O4-Ca-O4	82.30(10) (°)
Mn-O4-Mn	162.45(16) (°)		99.32(8) (°)

Fig. 4a reveals that the Dy doping induces an increase of the cell volume. Since Dy is much heavier than Ca, the calculated density shows also a strong increase. One can also observe that the a parameter increases whereas the c parameter decreases (Fig. 4b). As previously described, the substitution of Ca^{2+} by Dy^{3+} is electrically balanced by the reduction of an equivalent amount of Mn^{4+} in Mn^{3+} . According to Shannon, $R_{\text{Dy}^{3+}} < R_{\text{Ca}^{2+}}$ and $R_{\text{Mn}^{3+}} > R_{\text{Mn}^{4+}}$ [25]. Surprisingly, Fig. 4c highlights that the mean value of both Mn-O and (Ca,Dy)-O bond lengths increase with the doping level. However, all the Ca-O lengths do not follow the same behavior. Ca-O3 bond length along [001] decreases as expected (Fig. 4d). The shorter Ca-O4 bond increases whereas the longer one decreases (Fig. 4f). A quite similar behavior can be observed for the O4-Ca-O4 angles. The shorter one increases whereas the higher one remains unchanged (Fig. 4g). Such evolutions for the Ca-O4 bonds and O4-Ca-O4 angles induce a contraction of the Ca-Ca length and a tilt of the MnO_6 polyhedra around their [001] axes. Consequently, the Ca-O3 bond length perpendicular to [001] increases whereas it is expected to decrease if we only consider the ionic radius of Ca^{2+} and Dy^{3+} (Fig. 4e and h). It is interesting to note that the O3-Ca-O3 angle in the (001) plan remains unchanged whatever the doping level. Fig. 5 summarizes all these observations.

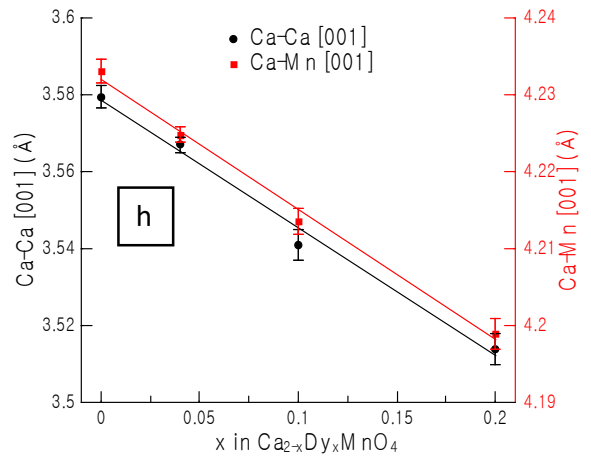
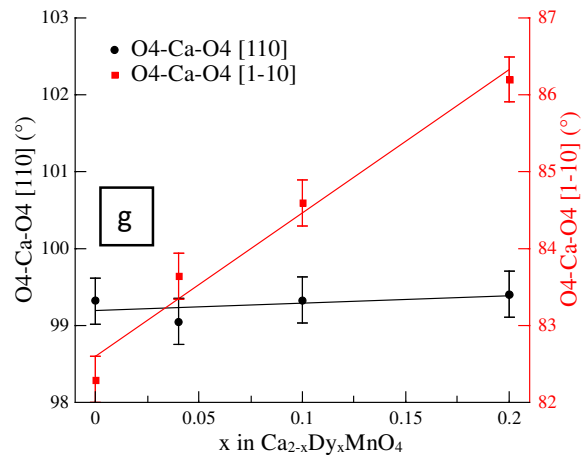
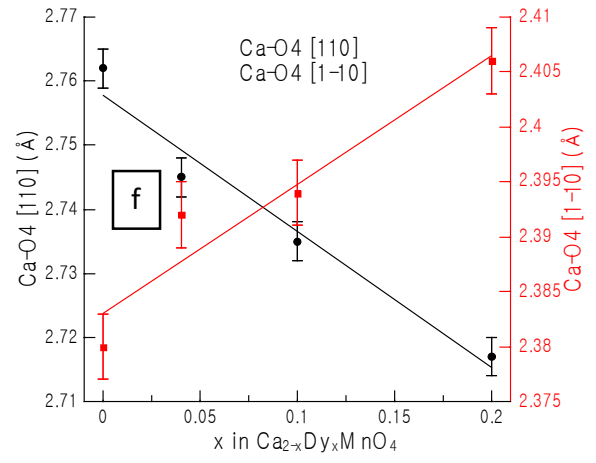
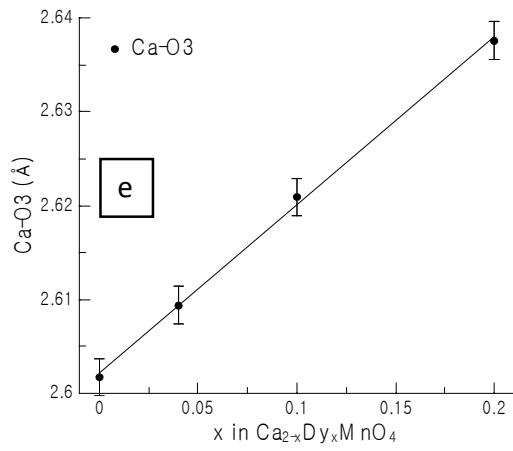
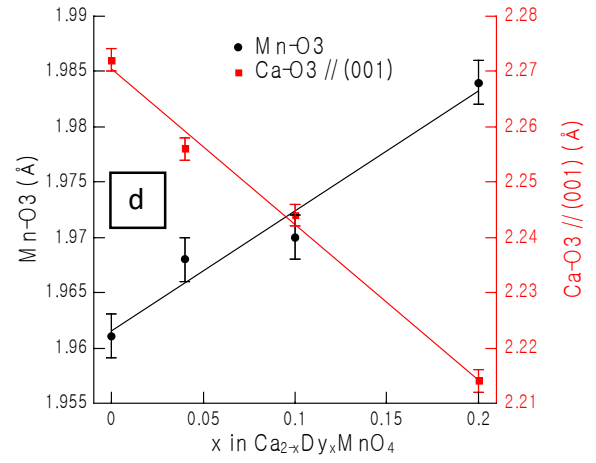
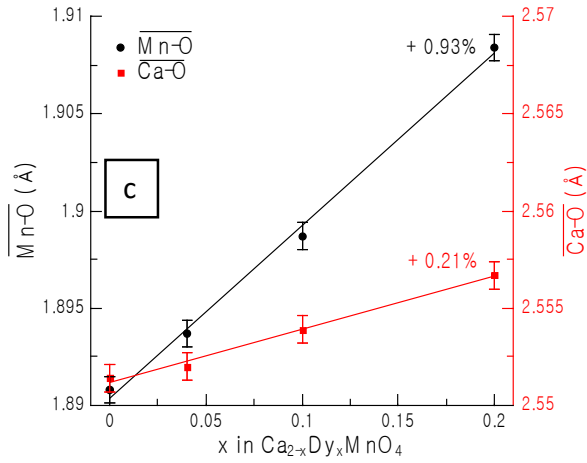
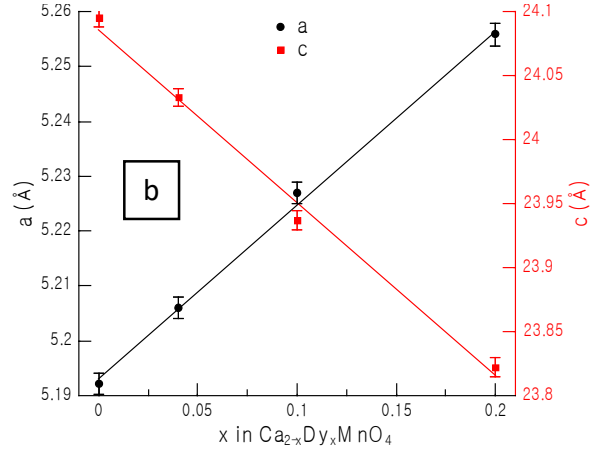
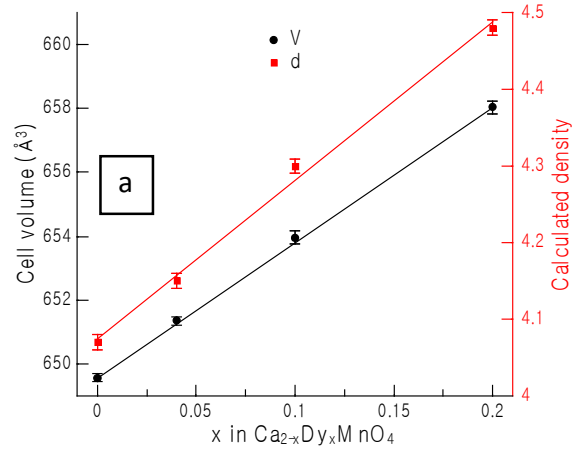


Fig. 4. Variation of different structural features of the $\text{Ca}_{2-x}\text{Dy}_x\text{MnO}_4$ structure as a function of Dy amount

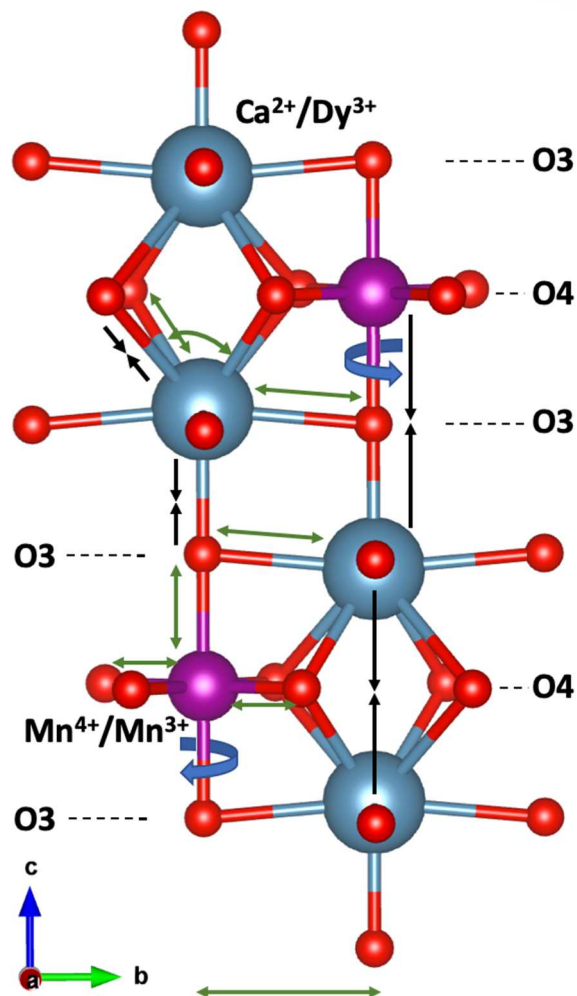


Fig. 5. Effect of Ca^{2+} substitution by Dy^{3+} on the crystal structure of $\text{Ca}_{2-x}\text{Dy}_x\text{MnO}_4$ in the range $0 < x < 0.2$

3.2. Thermal behavior

The thermal behavior of $\text{Ca}_{1.8}\text{Dy}_{0.2}\text{MnO}_4$ was investigated by the mean of the HT-X-ray diffraction method from room temperature to 800 °C. In this range, no phase transition was observed. Cell parameters, atomic positions and interatomic distances were determined by

Rietveld refinement of the HT XRD patterns. Thermal expansion coefficients α_x were calculated according to the following equation:

$$\frac{\Delta x}{x_0} = \alpha_x \Delta T \quad (2)$$

Where x is a cell parameter or an interatomic distance, x_0 the value at room temperature for the cell parameters and at 100 °C for the interatomic distances and T the temperature in K or °C.

Results are plotted in Fig. 6 and calculated thermal expansion coefficients are reported in Table 3.

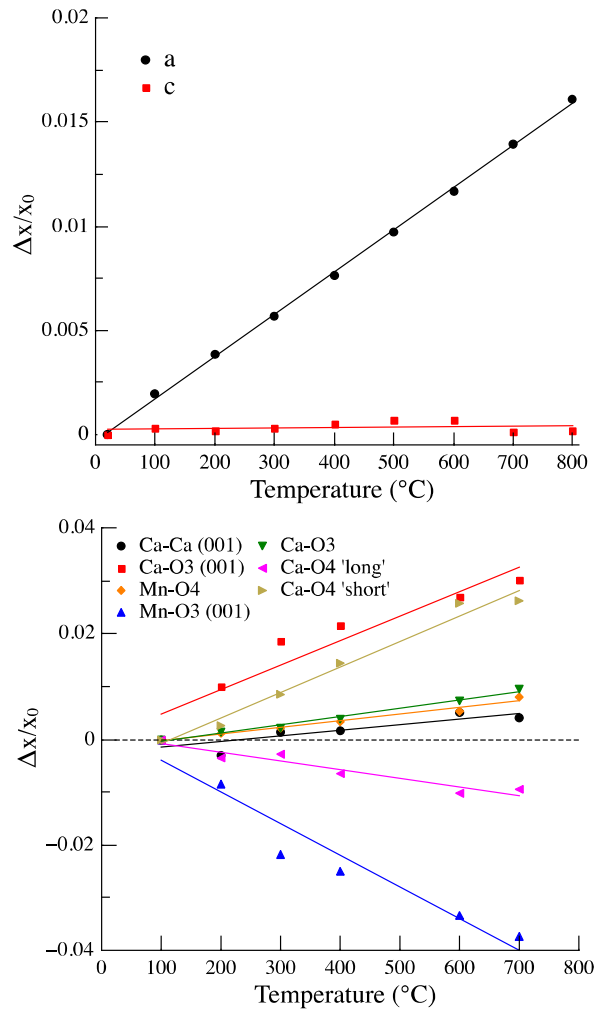


Fig. 6. Relative variations vs. temperature of the cell parameters (higher) and interatomic distances (lower) of $\text{Ca}_{1.8}\text{Dy}_{0.2}\text{MnO}_4$

Table 4

Thermal expansion coefficients of the cell parameters and interatomic distances of

$\text{Ca}_{1.8}\text{Dy}_{0.2}\text{MnO}_4$ (α_l is the calculated linear thermal expansion)

Bond	Thermal expansion coefficient (10^{-6} K^{-1})
α_a	20.3 ± 0.2
α_c	≈ 0
α_v	40.1 ± 0.5
$\alpha_l (=1/3 \alpha_v)$	13.7 ± 0.2
Ca-Ca	6 ± 0.5
Ca-Mn	-3.2 ± 0.6
Ca-O3 [001]	46 ± 7
Mn-O4	13 ± 1
Mn-O3 [001]	-60 ± 8
Ca-O3 (001)	15.6 ± 0.9
Ca-O4 'long'	-16 ± 2
Ca-O4 'short'	48 ± 4

The thermal expansion of $\text{Ca}_{1.8}\text{Dy}_{0.2}\text{MnO}_4$ is strongly anisotropic. Indeed, the thermal expansion coefficient along the a parameter is quite high compared to those classically observed for oxide materials (8 to $14 \times 10^{-6} \text{ K}^{-1}$ for a large majority of oxide-based materials). On the opposite, the thermal expansion along the [001] direction is negligible, resulting in a high thermal expansion anisotropy of $\Delta\alpha_{a-c} \approx 20 \times 10^{-6} \text{ K}^{-1}$.

The anisotropy in the thermal expansion coefficient of the $\text{Ca}_{2-x}\text{Dy}_x\text{MnO}_4$ structure can be explained by the analysis of the thermal behavior of the interatomic distances and the O-Ca-O angles (Fig. 6 and Table 4). All the results are summarized in Fig. 7.

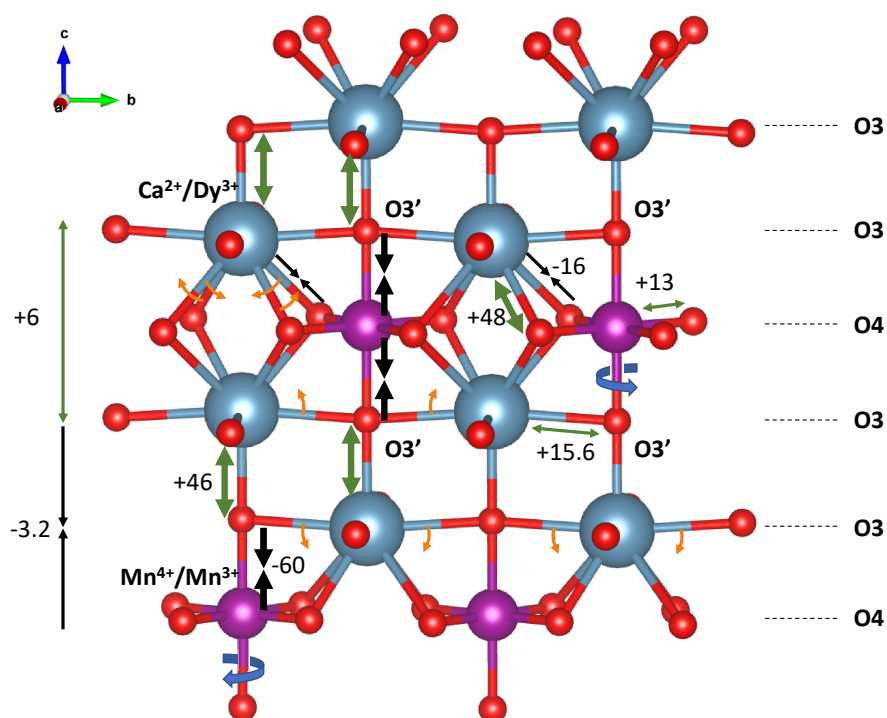


Fig. 7. Thermal evolution of the interatomic distances and O-Ca-O angles of the $\text{Ca}_{2-x}\text{Dy}_x\text{MnO}_4$ structure

Along the c axis, the cation-oxygen bonds exhibit a spectacular behavior, with a very strong thermal expansion for Ca-O3 ($+46 \times 10^{-6} \text{ K}^{-1}$) and a huge contraction for Mn-O3 ($-60 \times 10^{-6} \text{ K}^{-1}$). This leads to a flattening of the Ca-O3'-Ca angle in the (001) plane and a slight decrease of the Ca-Mn distance along [001]. The in (001) plane Mn-O4 bonds have a positive thermal expansion, resulting in a more regular MnO_6 octahedra. Similarly, the two Ca-O4 bonds show an opposite behavior, the shorter one expands on heating whereas the longer one contracts, allowing the MnO_6 octahedra to tilt around their [001] axis.

Covalent bonds between oxygen anions and small high-charge cations are generally faintly prone to expansion due to their high strength. For this reason, structures involving small regular polyhedra connected by corners, like many silicates, exhibit low cell expansion coefficients. Contrary to their p -block counterparts, high-charge transition cations are often surrounded by a distorted polyhedron that tends to achieve a more regular shape on heating,

like for example the TiO_6 octahedron in tetragonal BaTiO_3 . At low temperature, the MnO_6 octahedron of the present compound is stretched along the c-axis, resulting in an uneven distribution of the bond strengths between the (001) plane and the [001] axis (respectively $s_{\text{Mn-O4}} = 0.74$ and $s_{\text{Mn-O3}} = 0.50$ valence units (v.u.) calculated using Brese and O'Keeffe's model [26] at 100 °C). As a result, the difference reduces progressively (Fig. 8), while a convergence to a value near $2/3$ v.u. could be hypothesized by extrapolation of the experimental data around 1100 °C. Ideally, the increase of the two axial $s_{\text{Mn-O3}}$ (1.8×10^{-4} v.u.. $^{\circ}\text{C}^{-1}$) should be balanced by a -0.9×10^{-4} v.u.. $^{\circ}\text{C}^{-1}$ decrease of the four equatorial $s_{\text{Mn-O4}}$, but the slope measured for the latter is about twice lower ($-0.5 \cdot 10^{-4}$) in absolute terms. So, the cumulated bond strength around Mn seems to rise slightly but continuously from 3.95 to 4.06 v.u. with temperature, whereas it would be expected to decline due to thermal expansion. This phenomenon could result from the environment of the O4 atom (two short Mn-O bonds in the same (001) plane and four Ca-O ones out of the plane) as the so-formed flattened octahedron could allow transverse thermal oscillations of the anion. Although less efficient than in monodentate polyhedra arrays where thermal contraction can be observed [27,28], this mechanism is likely to attenuate the expansion of the Mn-O4 bond.

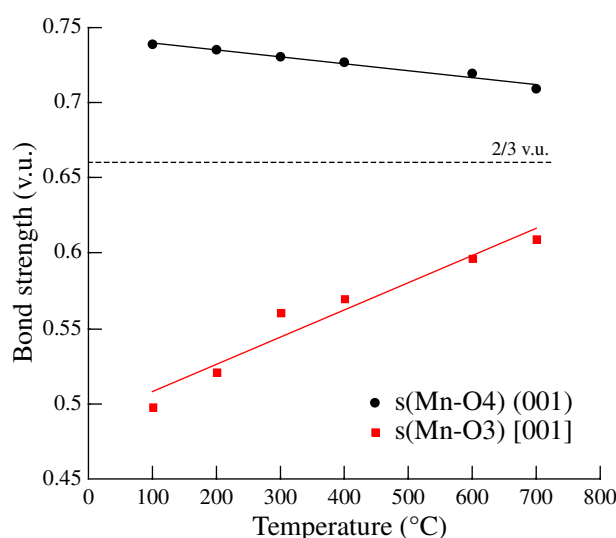


Fig. 8. Bond strength evolution vs. temperature for the two independent Mn-O bonds of $\text{Ca}_{1.8}\text{Dy}_{0.2}\text{MnO}_4$

HT-XRD also reveals a tendency to a higher cell symmetry at high temperature. In the present form, the Mn cations build a perfect square sublattice but the connecting O4 anions are located slightly off the mid-edge position. Their ordering result in a wide cell with $Z = 8$ formula units (Fig. 9, left). On heating however, O4 shifts progressively towards the ideal position, resulting in a homogenization of the Ca-O4 distances, hence the contraction of the long bonds and the expansion of the short ones. Conceivably, O4 may reach the mid-edge position at a temperature beyond the domain studied in this work. So, the four positions located around the $[001]$ axis would line up and the order would disappear (Fig. 9, right), resulting in a smaller cell ($(\mathbf{a} + \mathbf{b})/2$, $(\mathbf{a} - \mathbf{b})/2$, $\mathbf{c}/2$), $Z = 2$, space group $I4/mmm$), corresponding to the K_2NiF_4 archetype. This hypothesis is supported by the fact that numerous oxides are known to crystallize under this high-symmetry form ($\text{Ln}^{\text{III}}_2\text{M}^{\text{II}}\text{O}_4$ ($M = \text{Ni, Cu, Pd, ...}$), $\text{EA}^{\text{II}}\text{M}^{\text{IV}}_2\text{O}_4$ ($\text{EA} = \text{Ca, Sr, Ba; } M = \text{Ge, Ti, Sn, Ru, V, ...}$) and $\text{A}^{\text{I}}\text{M}^{\text{VI}}\text{O}_4$ ($\text{A} = \text{Na; } M = \text{Hg}$)), at room or high temperature [29,30,31].

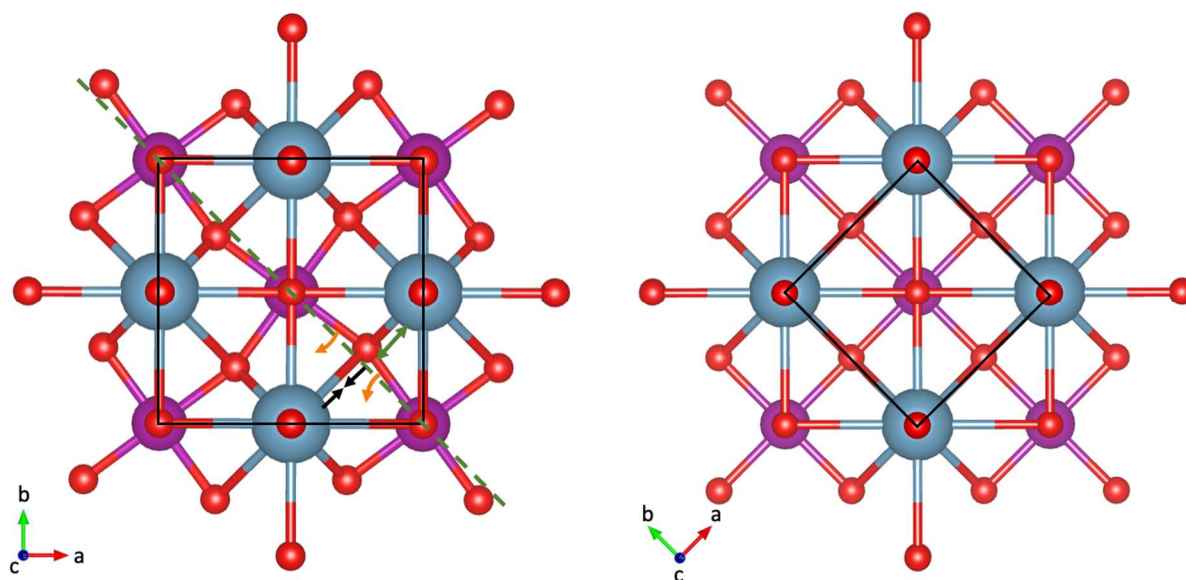


Fig. 9 The RT $I4_1/acd$ structure (left) of Ca_2MnO_4 would tend to a higher cell symmetry $I4/mmm$ (right) at high temperature

The resulting linear thermal expansion α_l of the studied compound $\text{Ca}_{1.8}\text{Dy}_{0.2}\text{MnO}_4$ is $13.7 \times 10^{-6} \text{ K}^{-1}$, which is a little bit less than that observed for CaMnO_3 calcium manganate ($15.6 \times 10^{-6} \text{ K}^{-1}$ [32]) and Sr_2TiO_4 Ruddlesden Popper ($19.5 \times 10^{-6} \text{ K}^{-1}$ at 327°C [33]). At the microstructure scale, the strong anisotropy in the thermal expansion coefficient of the $\text{Ca}_{2-x}\text{Dy}_x\text{MnO}_4$ structure must be considered with a great care since in these conditions, microcracking can occur when grain size exceeds a value called transition (or critical) grain size [34,35]. For example, the critical grain size for microcracking of $\text{Li}_{1.3}\text{Al}_{0.3}\text{Ti}_{1.7}(\text{PO}_4)_3$ is estimated to be less than or equal to $1.6 \mu\text{m}$ ($\Delta\alpha_{a-c} = 12 \times 10^{-6} \text{ K}^{-1}$) and to $1.1 \mu\text{m}$ for hydroxyapatite ($\Delta\alpha_{a-c} = 8 \times 10^{-6} \text{ K}^{-1}$) [36,37]. Consequently, the fabrication of dense and crack-free $\text{Ca}_{2-x}\text{Dy}_x\text{MnO}_4$ ceramics ($\Delta\alpha_{a-c} = 20 \times 10^{-6} \text{ K}^{-1}$) will be achieved only if the mean grain size could be maintained at a very low level, thus involving specific processing method, such as fast sintering or charge-assisted sintering. This would be also benefit for thermoelectric, mechanical and numerous other functional properties [38,39].

4. Conclusion

The effect of dysprosium doping on the crystal structure of the Ruddlesden-Popper phase $\text{Ca}_{2-x}\text{Dy}_x\text{MnO}_4$ at room temperature and its thermal behavior (for $x = 0.2$) in the range $\text{RT} - 800^\circ\text{C}$ were investigated in the range $0 < x < 0.2$ by Rietveld analysis of RT- and HT- X-ray powder diffraction data. The $I4_1/acd$ crystal structure is maintained in the whole investigated range, but Dy doping of Ca_2MnO_4 , electrically balanced by the reduction of an equivalent amount of Mn^{4+} in Mn^{3+} , induces a complex structural modification, leading to an increase of the a parameter and a decrease of the c one.

The thermal expansion of $\text{Ca}_{1.8}\text{Dy}_{0.2}\text{MnO}_4$ is strongly anisotropic with a $\Delta\alpha_{a-c} \approx 20 \times 10^{-6} \text{ K}^{-1}$. This is mainly driven by the tendency to a higher cell symmetry at high temperature of MnO_6 octahedra and by their tilt along their c -axis. The strong anisotropy in the thermal expansion

coefficient of the $\text{Ca}_{2-x}\text{Dy}_x\text{MnO}_4$ structure will imply to implement specific processes, such as flash sintering methods, in order to avoid critical microcracking in the material. This will be the point of a further work.

CRedit author statement

D. Bregiroux: Supervision, Conceptualization, Writing - Original draft preparation, Data curation, Funding acquisition, **A. Bahezre:** Investigation, Methodology, **M. Allani:** Investigation, Methodology, **G. Rouse:** Investigation, Formal analysis, Writing - review & editing, **G. Wallez:** Formal analysis, Writing - review & editing, **C. Laberty-Robert:** Supervision, Writing - review & editing.

Declaration of competing interest

The authors declare that they have no known competing financial interests or personal relationships that could have appeared to influence the work reported in this paper

Acknowledgements

This work was supported by the ANR NanoCerTex project, grant ANR-15-CE05-0013-01 of the French Agence Nationale de la Recherche

References

[1] R. Oka, T. Masui, Synthesis and characterization of black pigments based on calcium manganese oxides for high near-infrared (NIR) reflectance, RSC Adv. 6 (2016) 90952-90957. <https://doi.org/10.1039/C6RA21443F>

- [2] K. Tezuka, M. Inamura, Y. Hinatsu, Crystal structures and magnetic properties of $\text{Ca}_{2+x}\text{Sr}_x\text{MnO}_4$, *J. Solid State Chem.* 145 (1999) 705-710.
<https://doi.org/10.1006/jssc.1999.8290>
- [3] S.F. Matar, M.A. Subramanian, R. Weihrich, Ab initio investigation of the magnetic states of Ca_2MnO_4 and $\text{Ca}_2\text{MnO}_{3.5}$, *Chem. Phys.* 310 (2005) 231-238.
<https://doi.org/10.1016/j.chemphys.2004.10.035>
- [4] A. Castro-Couceiro, M. Sánchez-Andújar, B. Rivas-Murias, J. Mira, J. Rivas, M.A. Señarís-Rodríguez, Dielectric response in the charge-ordered $\text{Ca}_{2-x}\text{Pr}_x\text{MnO}_4$ phases, *Solid State Sci.* 7 (2005) 905-911. <https://doi.org/10.1016/j.solidstatesciences.2005.03.001>
- [5] J. Mira, A. Castro-Couceiro, M. Sánchez-Andújar, B. Rivas-Murias, J. Rivas and M.A. Señarís-Rodríguez, High dielectric constant in charge-ordered $\text{Ca}_{1.75}\text{Pr}_{0.25}\text{MnO}_4$, *J. Phys. D: Appl. Phys.* 39 (2006) 1192-1196. <https://doi.org/10.1088/0022-3727/39/6/027>
- [6] M.T. Tlili, N. Chihaoui, M. Bejar, E. Dhahri, M.A. Valente, E.K. Hlil, Charge ordering analysis by electrical and dielectric measurements in $\text{Ca}_{2-x}\text{Pr}_x\text{MnO}_4$ ($x = 0-0.2$) compounds, *J. Alloys Compd.* 509 (2011) 6447-6451. <https://doi.org/10.1016/j.jallcom.2011.03.088>
- [7] N. Chihaoui, M. Bejar, E. Dhahri, M.A. Valente, M.P.F. Graça, L.C. Costa, Dielectric relaxation of the $\text{Ca}_2\text{MnO}_{4-\delta}$ system, *J. Alloys Compd.* 577S (2013) S483-S487.
<https://doi.org/10.1016/j.jallcom.2012.03.039>
- [8] Y. Surace, M. Simões, J. Eilertsen, L. Karvonen, S. Pokrant, A. Weidenkaff, Functionalization of $\text{Ca}_2\text{MnO}_{4-\delta}$ by controlled calcium extraction: Activation for electrochemical Li intercalation, *Solid State Ion.* 266 (2014) 36-43.
<https://doi.org/10.1016/j.ssi.2014.08.005>
- [9] L. Bocher, M. H. Aguirre, D. Logvinovich, A. Shkabko, R. Robert, M. Trottman, and A. Weidenkaff, $\text{CaMn}_{1-x}\text{Nb}_x\text{O}_3$ ($x \leq 0.08$) perovskite-type phases as promising new high-

temperature n-type thermoelectric materials, *Inorg. Chem.* 47 (2008) 8077-8085.

<https://doi.org/10.1021/ic800463s>

[10] A. Baranovskiy, A. Graff, J. Klose, J. Mayer, Y. Amouyal, On the origin of vibrational properties of calcium manganate based thermoelectric compounds, *Nano Energy* 47 (2018) 451-462. <https://doi.org/10.1016/j.nanoen.2018.02.054>

[11] A. Azulay, Y. Amouyal, Tailoring electronic and thermal transport properties of $\text{CaO}(\text{CaMnO}_3)_m$ -based ($m = 1$ and $m = \infty$) composites for thermoelectric power generation, *Acta Mater.* 164 (2019) 481-492. <https://doi.org/10.1016/j.actamat.2018.10.052>

[12] I.D. Fawcett, J.E. Sunstrom IV, and M. Greenblatt, M. Croft, K.V. Ramanujachary, Structure, magnetism, and properties of Ruddlesden-Popper calcium manganates prepared from citrate gels, *Chem. Mater.* 10 (1998) 3643-3651. <https://doi.org/10.1021/cm980380b>

[13] F. Kawashima, X.Y. Huang, K. Hayashi, Y. Miyasaki, T. Kajitani, Structure and high-temperature thermoelectric properties of the n-Type layered oxide $\text{Ca}_{2-x}\text{Bi}_{x-\delta}\text{MnO}_{4-\gamma}$, *J. Electron Mater.* 38 (2009) 1159-1162. <https://doi.org/10.1007/s11664-009-0700-z>

[14] N. Chihaoui, R. Dhahri, M. Bejar, E. Dharhi, L.C. Costa, M.P.F. Graça, Electrical and dielectric properties of the $\text{Ca}_2\text{MnO}_{4-\delta}$ system, *Solid State Commun.* 151 (2011) 1331-1335. <https://doi.org/10.1016/j.ssc.2011.06.023>

[15] A. Baranovskiy, Y. Amouyal, Structural stability of calcium-manganate based $\text{CaO}(\text{CaMnO}_3)_m$ ($m = 1, 2, 3, \infty$) compounds for thermoelectric applications, *J. Alloys Compd.* 687 (2016) 562-569. <http://dx.doi.org/10.1016/j.jallcom.2016.06.141>

[16] J. Hea, Y. Liu, R. Funahashi, Oxide thermoelectrics: The challenges, progress, and outlook, *J. Mater. Res.* 26 (2011) 1762-1772. <https://doi.org/10.1557/jmr.2011.108>

[17] J. Takahashi, N. Kamegashira, X-ray structural study of calcium manganese oxide by rietveld analysis at high temperatures [$\text{Ca}_2\text{MnO}_{4.00}$], *Mater. Res. Bull.* 28 (1993) 565-573. [https://doi.org/10.1016/0025-5408\(93\)90053-G](https://doi.org/10.1016/0025-5408(93)90053-G)

- [18] C. Chaumont, A. Daoudi, G. Le Flem, P. Hagenmuller, Préparation, propriétés cristallographiques, magnétiques et électriques de la solution solide $\text{Ca}_{2-x}\text{Y}_x\text{MnO}_4$, J. Solid State Chem. 14 (1975) 335-341. [https://doi.org/10.1016/0022-4596\(75\)90052-3](https://doi.org/10.1016/0022-4596(75)90052-3)
- [19] Y. Wang, Y. Sui, and W. Su, High temperature thermoelectric characteristics of $\text{Ca}_{0.9}\text{R}_{0.1}\text{MnO}_3$ (R = La, Pr, ..., Yb), J. Appl. Phys. 104 (2008) 93703-93709. <http://dx.doi.org/10.1063/1.3003065>
- [20] B. Zhan, J. Lan, Y. Liu, Y. Lin, Y. Shen, C. Nan, High temperature thermoelectric properties of Dy-doped CaMnO_3 ceramics, J. Mater. Sci. Technol. 30 (2014) 821-825. <http://dx.doi.org/10.1016/j.jmst.2014.01.002>
- [21] J. Rodriguez-Carvajal, FULLPROF: A Program for Rietveld Refinement and Pattern Matching Analysis, In Satellite meeting on powder diffraction of the XV congress of the IUCr 127 (1990). Program available at <https://www.ill.eu/sites/fullprof/>
- [22] M. E. Leonowicz, K. R. Poeppelmeier, J. M. Longo, Structure determination of Ca_2MnO_4 and $\text{Ca}_2\text{MnO}_{3.5}$ by X-ray and neutron methods, J. Solid State Chem. 59 (1985) 71-80. [https://doi.org/10.1016/0022-4596\(85\)90352-4](https://doi.org/10.1016/0022-4596(85)90352-4)
- [23] C. Autret, C. Martin, M. Hervieu, R. Retoux, B. Raveau, G. André, F. Bourée, Structural investigation of Ca_2MnO_4 by neutron powder diffraction and electron microscopy, J. Solid State Chem. 177 (2004) 2044-2052. <https://doi.org/10.1016/j.jssc.2004.02.012>
- [24] L.W. Finger, D.E. Cox, A.P. Jephcoat, A correction for powder diffraction peak asymmetry due to axial divergence, J. Appl. Cryst. 27 (1994) 892-900. <https://doi.org/10.1107/S0021889894004218>
- [25] R.D. Shannon, Revised effective ionic radii and systematic studies of interatomic distances in halides and chalcogenides, Acta Crystallogr. A32 (1976) 751-767. <https://doi.org/10.1107/S0567739476001551>

- [26] N. E. Brese, M. O'Keeffe, Bond-valence parameters for solids, *Acta Cryst.* B47 (1991) 192-197. <https://doi.org/10.1107/S0108768190011041>
- [27] A. W. Sleight, Compounds that contract on heating, *Inorg. Chem.* 37 (1998) 2854-2860. <https://doi.org/10.1021/ic980253h>
- [28] C. Lind, Two decades of negative thermal expansion research: where do we stand?, *Materials* 5 (2012) 1125-1154. <https://doi.org/10.3390/ma5061125> [open access]
- [29] S.J. Skinner, Characterization of $\text{La}_2\text{NiO}_{4+\delta}$ using in-situ high temperature neutron powder diffraction, *Solid State Sci.* 5 (2003) 419-426. [https://doi.org/10.1016/S1293-2558\(03\)00050-5](https://doi.org/10.1016/S1293-2558(03)00050-5)
- [30] D. Ninga, A. Bakia, T. Scherb, J. Song, A. Fantin, X. Liu, G. Schumacher, J. Banhart, H.J.M. Bouwmeester, Influence of A-site deficiency on structural evolution of $\text{Pr}_{2-x}\text{NiO}_{4+\delta}$ with temperature, *Solid State Ion.* 342 (2019) 115056. <https://doi.org/10.1016/j.ssi.2019.115056>
- [31] G. Nirala, D. Yadav, S. Upadhyay, Ruddlesden–Popper phase A_2BO_4 oxides: Recent studies on structure, electrical, dielectric, and optical properties, *J. Adv. Ceram.* 9 (2020) 129-148. <https://doi.org/10.1007/s40145-020-0365-x>
- [32] C. Boonsri, P. Limsuwan, P. Buranasiri, Determination of thermal expansion coefficient for thermoelectric CaMnO_3 with a shadow method, *Ukr. J. Phys. Opt.* 21(1) (2020) 26-34. <https://doi.org/10.3116/16091833/21/1/26/2020>
- [33] L.-F. Huang, N. Z. Koocher, M. Gu, J. M. Rondinelli, Structure dependent phase stability and thermal expansion of Ruddlesden-Popper strontium titanates, *Chem. Mater.* 30 (2018) 7100-7110. <https://doi.org/10.1021/acs.chemmater.8b02944>
- [34] D. Bregiroux, J. Cedelle, I. Ranc, C. Barreateau, G. Mata Osoro, G. Wallez, Effect of the sintering method on microstructure and thermal and mechanical properties of zirconium

oxophosphate ceramics $\text{Zr}_2\text{O}(\text{PO}_4)_2$, J. Phys. Chem. Solid 111 (2017) 304-310.

<http://dx.doi.org/10.1016/j.jpcs.2017.08.008>

[35] M. Tomczyk, A.M.O.R. Senos, I.M. Reaney and P.M. Vilarinho, Reduction of microcracking in YMnO_3 ceramics by Ti substitution, Scripta Mater. 67 (2012) 427-430.

<https://doi.org/10.1016/j.scriptamat.2012.04.042>

[36] T. P. Hoepfner, E. D. Case, An estimate of the critical grain size for microcracks induced in hydroxyapatite by thermal expansion anisotropy, Mater. Lett. 58 (2004) 489-492.

[https://doi.org/10.1016/S0167-577X\(03\)00531-7](https://doi.org/10.1016/S0167-577X(03)00531-7)

[37] S. D. Jackman, R. A. Cutler, Effect of microcracking on ionic conductivity in LATP, J. Power Sources 218 (2012) 65-72. <https://doi.org/10.1016/j.jpowsour.2012.06.081>

[38] M. Gunes, M. Ozenbas, Effect of grain size and porosity on phonon scattering enhancement of $\text{Ca}_3\text{Co}_4\text{O}_9$, J. Alloys Compd. 626 (2015) 360-367.

<https://doi.org/10.1016/j.jallcom.2014.12.004>

[39] K.R. Kambale, Akash Mahajan, S.P. Butee, Effect of grain size on the properties of ceramics, Met. Powder Rep., 74 (2019) 130-136. <https://doi.org/10.1016/j.mprp.2019.04.060>

